Quadratic magnetoelectric effect during field cooling in sputter grown Cr_2O_3 films

Muftah Al-Mahdawi,[1,2,*] Tomohiro Nozaki,[3,†] Mikihiko Oogane,[1,2,4] Hiroshi Imamura,[3] Yasuo Ando,[1,2,4] and Masashi Sahashi[5]

[1]*Center for Science and Innovation in Spintronics (Core Research Cluster), Tohoku University, Sendai, 980-8577, Japan*
[2]*Center for Spintronics Research Network, Tohoku University, Sendai 980-8577, Japan*
[3]*Research Center for Emerging Computing Technologies, National Institute of Advanced Industrial Science and Technology (AIST), Tsukuba 305-8568, Japan*
[4]*Department of Applied Physics, Tohoku University, Sendai 980-8579, Japan*
[5]*School of Engineering, Tohoku University, Sendai 980-8579, Japan*

(Received 3 November 2020; revised 16 August 2021; accepted 2 September 2021; published 14 September 2021)

Cr_2O_3 is the archetypal magnetoelectric (ME) material, which has a linear coupling between electric and magnetic polarizations. Quadratic ME effects are forbidden for the magnetic point group of Cr_2O_3, due to space-time inversion symmetry. In Cr_2O_3 films grown by sputtering, we find a signature of a quadratic ME effect that is not found in bulk single crystals. We use Raman spectroscopy and magnetization measurements to deduce the removal of space-time symmetry and corroborate the emergence of the quadratic ME effect. We propose that metastable site-selective trace dopants remove the space, time, and space-time inversion symmetries from the original magnetic point group of bulk Cr_2O_3. We include the quadratic ME effect in a model describing the switching process during ME field cooling and estimate the effective quadratic susceptibility value. The quadratic magnetoelectric effect in a uniaxial antiferromagnet is promising for multifunctional antiferromagnetic and magnetoelectric devices that can incorporate optical, strain-induced, and multiferroic effects.

DOI: 10.1103/PhysRevMaterials.5.094406

I. INTRODUCTION

The coupling between the magnetic and electric orders in single-phase materials is interesting for fundamental physics research and applications in multifunctional multi-input information storage and processing devices [1]. The magnetoelectric (ME) effect arises in the expansion of the thermodynamic potential as coupling terms between the electric E and magnetic H fields [2]. The linear ME effect was theoretically predicted and experimentally observed first in the antiferromagnet corundum-type Cr_2O_3 [2–4] and later found renewed interest in ME-type memory [5–7]. Higher-order ME effects that are quadratic in E or H have been found in various materials [8–12]. Equivalent to quadratic ME effects, the linear magneto-optical effect was also found for other antiferromagnets [13]. However, the simultaneous presence of quadratic and linear ME effects in the same material phase is not frequently found. A necessary condition of the linear ME effect is the symmetry breaking of a magnetic crystal under space-inversion (I) and time-reversal (R) operations [14,15]. The quadratic ME effects require a breaking of space-time inversion (IR) symmetry and either I or R symmetry [15,16]. Understanding of the interplay between linear and nonlinear ME effects will be of interest for applications in ME memory and devices.

Cr_2O_3 has the same rhombohedral crystal structure as corundum α-Al_2O_3, with the crystallographic point group of $\bar{3}m$. Cr^{3+} cations fill 2/3 of distorted O^{2-} anion octahedra. The Cr cations lie along the $\bar{3}$ axis, with an inversion center in an empty octahedron, and the O anions lie on the $2/m$ axes. Above the Néel temperature of Cr_2O_3 ($T_N = 307$ K), the spin configuration is paramagnetic, and the magnetic point group (MPG) is the gray $\bar{3}m1'$, where the individual I and R symmetries are present, similar to the parent corundum rhombohedral crystal. Upon the magnetic ordering below T_N, the MPG is lowered to $\bar{3}'m'$, which breaks the single I and R symmetries [2]. There are two distinct spin configurations of $\downarrow\uparrow\cdot\downarrow\uparrow$ (L^+ domain state) and $\uparrow\downarrow\cdot\uparrow\downarrow$ (L^- domain state), where the dot denotes the inversion center. The order parameter is the antiferromagnetic order vector, defined from the four Cr spins as $\ell = s_1 - s_2 + s_3 - s_4$ [Fig. 1(a)]. Both ℓ and the linear ME susceptibility α change signs under I and R operations. In the convention used by Birss [17] (discussed by Grimmer [18]), both ℓ and α are $-c$ tensors, and they are commensurate with each other.

The ME effect can be expanded with higher-order terms. The quadratic effects are represented by the energy terms βEH^2 for the electrobimagnetic effect and γHE^2 for the magnetobielectric effect. The third-rank susceptibility tensors β and γ have nonvanishing components in MPGs that permit piezoelectricity and piezomagnetism, respectively [19]. The MPG $\bar{3}'m'$ of Cr_2O_3 has the combined IR symmetry [2], as shown in Fig. 1(a). The presence of IR symmetry permits the linear ME effect but forbids the quadratic ME effects and the various pyro-, ferro-, or piezoelectric and magnetic effects. This condition can be seen in the effect of IR operation on the relevant ME energy terms in the expanded thermodynamic

*mahdawi@tohoku.ac.jp
†nozaki.tomohiro@aist.go.jp

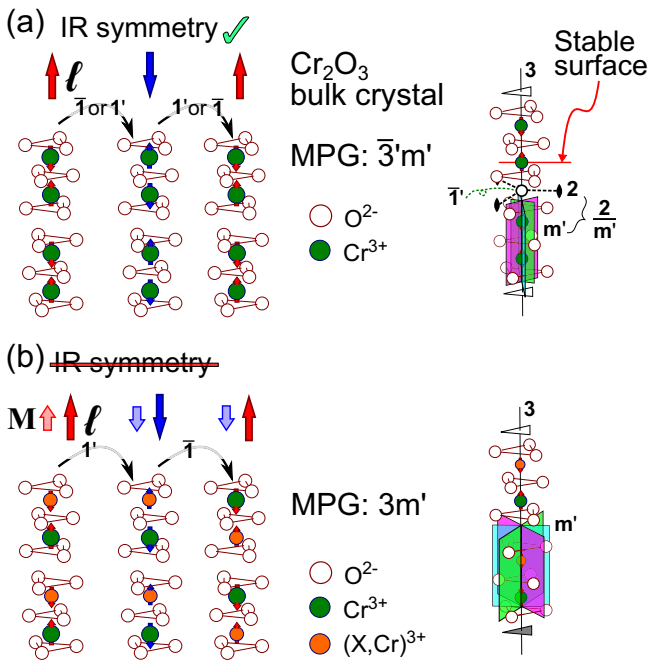

FIG. 1. (a) The spin configuration of Cr_2O_3 breaks either the $I \equiv \bar{1}$ or $R \equiv 1'$ symmetries, but it is symmetric under the combined $IR \equiv \bar{1}'$ operation. (b) We propose that the presence of nonequivalent spin moments breaks the combined IR symmetry, which results in an uncompensated magnetization M and quadratic ME effects. Schematics of magnetic point groups $\bar{3}'m'$ and $3m'$ for each case are shown on the right side.

potential energy F, as follows:

$$F = -\alpha EH - \tfrac{1}{2}\beta EH^2 - \tfrac{1}{2}\gamma E^2 H + \cdots,$$
$$(R \circ I)(F) - F = +\beta EH^2 + \gamma E^2 H. \quad (1)$$

The presence of IR symmetry imposes $(R \circ I)(F) - F = 0$, and the quadratic ME effects are prohibited. For more details and forms of tensors, we refer to the reviews in Refs. [15,20–22] and the original works in Refs. [16,18,19,23,24].

In this paper, we found evidence of a quadratic ME effect in sputtered Cr_2O_3 films, which is not permitted in the MPG $\bar{3}'m'$ of bulk Cr_2O_3. We propose that the presence of nonequivalent spin moments at each sublattice removes the IR symmetry, and the MPG will be $3m'$ [Fig. 1(b)]. First, we clarify the lack of I, R, and IR symmetries from measurements of the thermoremnant magnetization and Raman spectroscopy. After that, we investigate the quadratic ME effect from measurements of the domain switching probability during the ME field cooling (MEFC) process. Then, we use this procedure to estimate the relative magnitude of the quadratic ME effect in our sample.

II. EXPERIMENTAL DETAILS

We used samples similar to those used in earlier reports [25–28]. The reference sample is a c-cut bulk single-crystal substrate, having dimensions of $4 \times 4 \times 0.5\,rmmm^3$, prepared by the Verneuil process and acquired commercially. The film samples had the stack structure of Al_2O_3-(0001) substrate/Pt 25 nm/Cr_2O_3-(0001) 500, 1000, and 2300 nm/no capping, where the numbers are the layer nominal thicknesses. The Pt layer was grown by dc magnetron sputtering, and the Cr_2O_3 film layer was grown by reactive rf magnetron sputtering from a metallic Cr target (99.99% purity) in a mixture of argon and oxygen gases. The growth substrate temperature of Cr_2O_3 and Pt layers was kept relatively low at 773 K, to preserve the metastable structure.

The determination of the symmetry elements by crystal diffraction techniques is unfeasible. X-ray or neutron-based diffraction methods determine only the Laue class and cannot determine the presence or absence of I symmetry in our Cr_2O_3 films (Sec. S1 in Ref. [29]). On the other hand, vibrational spectra are sensitive to the I symmetry of the crystallographic point group. Also, magnetization and magnetoelectric effects are determined by the R and IR symmetries. We measured the thermoremnant magnetizations and Raman spectra to infer which symmetries are removed from the original Cr_2O_3 MPG of $\bar{3}'m'$.

We characterized the thermoremnant magnetic properties using a superconducting quantum interference device (SQUID) magnetometer, where we measured the magnetization along the out-of-plane direction, parallel to the c axis. After a field cooling in a magnetic field $H_{fr} = 10$ kOe from 330 K down to 10 K, we set the magnetic field to zero, and we measured the magnetization in the heating direction at 1 K/min heating rate. We measured Raman scattering in the same samples at room temperature ≈293 K. We used a micro-Raman spectrometer, equipped with a green laser ($\lambda = 532.133$ nm, 50 mW), and measured in the $\bar{Z}(YY)Z$ backscattering geometry configuration. We set the span of the Raman shift at 200–2500 cm^{-1}, with a resolution of 6.8 cm^{-1}. The Pt bottom layer blocks the laser beam, and no Raman scattering was detected from the sapphire substrate.

We measured the ME properties of two other samples. The first is a bulk single crystal metallized on both (0001) faces by Ta 10 nm/Cu 300 nm electrodes. The second is Al_2O_3 substrate/Pt 25 nm/Cr_2O_3 500 nm/Pt 25 nm fabricated into a 4×2-mm^2 cross-capacitor structure. We characterized the average domain configurations by the converse ME effect, where the electrically induced magnetization was measured by lock-in detection in a SQUID magnetometer. More details of the measurement setup are described elsewhere [25].

III. SYMMETRY IN SPUTTERED Cr_2O_3 FILMS

Figure 2(a) shows the thermoremnant magnetization measurements, at zero field after field cooling. The temperature dependence shows pyromagnetism, and the transition temperature coincides with the T_N of Cr_2O_3. The magnetization areal density scales linearly with the film thickness [inset of Fig. 2(a)], showing that the magnetization is within the volume of the films. The estimated low-temperature magnetization value is very low at 0.06 emu/cm^3.

A finite magnetization in Cr_2O_3 films was reported before. It was attributed to uncompensated moments at the films surface, either by interfacial misfit dislocations [30] or by the boundary magnetization due to removal of I symmetry at the surface [31,32]. In contrast, we found that sputtered Cr_2O_3 films have volume pyromagnetism, likely of a ferrimagnetic-type origin [25–28,33]. The magnitude of M and the sign of

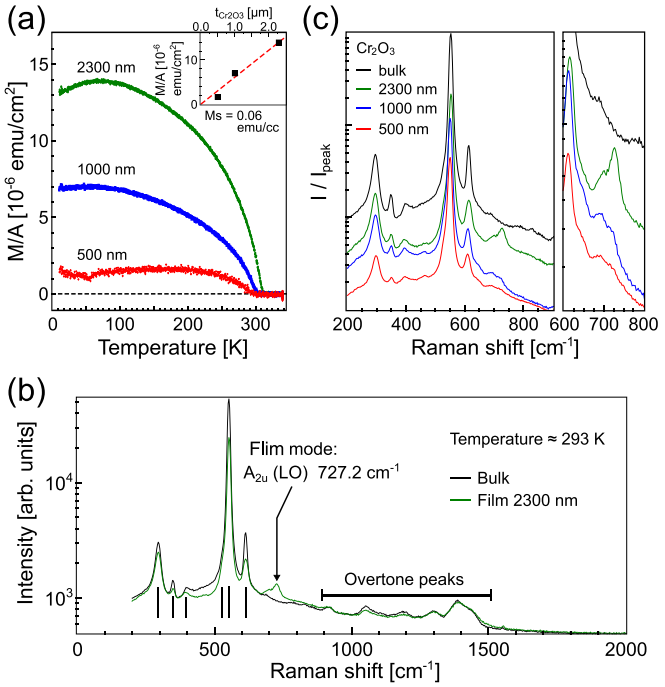

FIG. 2. (a) Temperature dependence of thermoremnant magnetization in the sputtered Cr_2O_3 films. The inset shows the scaling of areal magnetization density (M/A) with thickness, where the slope is the volume magnetization (M_s). (b) The wide-span Raman spectra of the bulk and 2300-nm samples. The locations of Raman modes are listed in Table I. (c) Comparison of the Raman spectra. An enlarged view of the 727.2-cm^{-1} mode is in the right panel.

$\ell \cdot M$ can be controlled by dopant concentration and type. For example, we found that aluminium doping results in a parallel orientation between ℓ and M. At 0.07% Al doping level, we had $M = 2$ emu/cm^3, and it reached up to 60 emu/cm^3 at 3.7% Al doping level [28]. In the present results, the Cr_2O_3 films are nominally nondoped, but the pyromagnetism origin is the same. There are trace dopants present in the sputtering deposition targets or chamber walls, which are incorporated in the films. We have a volume magnetization of 0.06 emu/cm^3, which corresponds to a doping level of 35 ppm. The high-purity sputtering targets have a guaranteed purity at the 100-ppm level. The trace elements are likely to be Al and Si, based on the origin of target materials. Therefore even nominally nondoped films have a ferrimagnetic-type volume pyromagnetism.

Ferro- and ferrimagnetism are allowed only if the MPG is a subgroup of ∞/mm' [21]. Magnetic crystals with either R or IR symmetries cannot support ferromagnetism. The MPG $\bar{3}'m'$ of bulk Cr_2O_3 has IR symmetry [2]. To remove the IR symmetry, nonequivalent spin moments at each sublattice are required, and the MPG will be $3m'$ [Fig. 1(b)]. Cation dopants in Cr_2O_3 substitute the host Cr sites [34,35]. Site-selective substitution by nonmagnetic dopants reduces one of the sublattice magnetic moments on average and/or induces ion displacement by chemical pressure. The corundum-type crystals have a surface that is stable if terminated in the bottom half of the buckled metal-ion layer, as indicated in Fig. 1(a) [36–39]. The topmost Cr ion has a large relaxation towards the oxygen plane, and

TABLE I. Identified modes in Raman spectra of Cr_2O_3 bulk and film samples. Note that the fourth-mode position values cannot be determined due to the large peak of A_{1g} mode and they are for indication only.

	Raman shift (cm^{-1})			
Mode	Bulk	2300 nm	1000 nm	500 nm
E_g or A_{1g}	295.2	295.0	295.9	297.6
E_g	348.9	350.0	349.8	350.6
E_g	398.1	394.1	394.5	395.0
E_g	(528)	(520)	(520)	(521)
A_{1g}	552.4	553.2	550.2	549.8
E_g	613.7	614.5	611.0	610.2

the oxidation state is close to Cr^{2+}, instead of Cr^{3+} of the bulk [37,38]. The surface electrostatic environment is closer to a lithium niobate ($LiNbO_3$)-type environment, and the occupation energy does not become equivalent to the dopant and Cr ions. Therefore a metastable site-selective substitution accumulates during the layer-by-layer growth of doped Cr_2O_3 films, under relatively low growth temperatures. The resulting MPG below T_N becomes $3m'$, instead of $\bar{3}'m'$ [Fig. 1(b)]. This is only observed for a layered film growth mechanism, and not for films prepared by postannealing [40] or bulk doped-Cr_2O_3 powders; cf. the supplementary information of Ref. [28]. In the $3m'$ MPG, the α tensor has the same form as that in the $\bar{3}'m'$ MPG. This explains why the α in Cr_2O_3 films is similar to that of the bulk single crystal in magnitude and temperature dependence, regardless of doping [25,28,33,41].

The proposition of site-selective substitution has the I symmetry removed also from the parent crystallographic point group, as seen after the I operation in Fig. 1(b). This makes our Cr_2O_3 films polar, even in the paramagnetic phase, similar to lithium niobate. In vibrational spectra, when an I symmetry is present in the parent crystallographic point group, there is a mutual exclusion between the Raman-active and infrared-active (ir-active) vibrational modes. In a rhombohedral corundum crystal, the irreducible representation of the optical modes is [42–45]

$$\Gamma_{\text{opt}} = 2A_{1g} + 5E_g + 2A_{2u} + 4E_u + 2A_{1u} + 3A_{2g}. \quad (2)$$

The Raman-active modes are two A_{1g} and five E_g modes, the ir-active modes are two A_{2u} and four E_u modes, and three A_{2g} and two A_{1u} modes are silent. In Fig. 2(b), we show a comparison between the wide-span Raman spectra of the bulk and 2300-nm samples. We note that the measurement temperature is room temperature, and the focused laser spot heats the local temperature above T_N. Thus the Raman spectra are acquired in the paramagnetic phase. All the peaks in the bulk sample can be assigned to the reference values in the literature, even though there is no agreed-upon consensus on each of them [46]. The film sample has an identical spectrum for most of the peaks. The Pt buffer layer increases the collection of scattered light and results in a high-intensity spectrum. In Fig. 2(c), we show the Raman spectra acquired from the same samples as in Fig. 2(a), and we list the position of our measured modes in Table I. The peak positions of the films are

close to the bulk values, indicating that the films are relaxed with negligible stress [43,47].

A new mode at a Raman shift of 727.2 cm^{-1} appears only in the film samples [identified by an arrow in Fig. 2(b)]. This mode also increases in intensity with increasing film thickness [right panel of Fig. 2(c)]. In Cr_2O_3, the most intense modes are the phonon modes of A_{1g} and A_{2u} [48,49]. The films' new mode at 727.2 cm^{-1} can be identified with a A_{2u} longitudinal-optical (LO) mode [48], which should be an ir-active, Raman-inactive mode. The site-selective substitution in Cr_2O_3 films removes the centrosymmetry of the parent rhombohedral point group, and the rule of mutual exclusion does not hold. The A_{1g} and A_{2u} modes will have A_1-symmetry character, and both become Raman active. Similar findings of activation of ir-only modes were found in Cr_2O_3-Fe_2O_3 solid solutions [49] and in pure Cr_2O_3 at ambient pressure after applying 61 GPa [46], and they were attributed to symmetry lowering. Two additional weak peaks appear for the films at 462 and 693 cm^{-1}. The positions of these modes coincide with A_2-symmetry modes from first-principles calculations [50]. When centrosymmetry is removed, the silent A_{1u} and A_{2g} modes become A_2 in symmetry, which is still silent for both Raman and ir spectroscopy. However, the A_2 modes are active for the two-photon hyper-Raman scattering, which is a significantly weak scattering process. A possible explanation is that resonant enhancement of hyper-Raman scattering occurs when the two-photon pumping energy aligns with an electronic transition [51,52]. The peaks at 916, 1050, 1181, 1300, 1386, and 1440 cm^{-1} are present for both sputtered films and the single-crystal substrate. They are the first overtones or combinations of the fundamental modes [49], which can be Raman active even if the fundamental mode is silent.

The combination of magnetization and Raman spectra measurements shows that the I, R, and IR symmetries are removed from the magnetically ordered phase and the I symmetry is removed from the paramagnetic phase. The oxygen octahedra present mirror-primed symmetry elements. Based on the relaxation of the films, we do not expect a significant distortion to the oxygen octahedra. Therefore the MPG of our sputtered Cr_2O_3 is only lowered from $\bar{3}'m'$ to $3m'$. If the oxygen octahedra have vacancies, the MPG will be further lowered to 3. In either case, quadratic and linear ME effects are allowed.

IV. QUADRATIC ME EFFECT OF Cr_2O_3 DURING FIELD COOLING

In the textured Cr_2O_3 films, the final domain state after MEFC is governed by the short-range-ordered activation domains near T_N [25,53]. The average domain state $\langle L\rangle$ is found from the average linear ME response of the sample, normalized to the saturation value ($\langle L\rangle = \alpha_{\rm meas}/\alpha_{\rm max}$). $\langle L\rangle$ can be defined from the Boltzmann distribution (P_Θ) of the instantaneous angle θ of ℓ with the c axis as a function of the microscopic free energy W at T_N, as follows [25,26]:

$$P_\Theta(\theta) \propto \sin\theta \exp\left(\frac{-W(\theta)}{k_B T_N}\right), \tag{3}$$

$$\langle L\rangle = \frac{\alpha_{\rm meas}}{\alpha_{\rm max}} \equiv \frac{\int_0^\pi \mathrm{sgn}(\cos\theta) P_\Theta(\theta) d\theta}{\int_0^\pi P_\Theta(\theta) d\theta}, \tag{4}$$

where $\mathrm{sgn}(\cos\theta)$ is the signum function, which gives the opposite sign to each domain state, and k_B is the Boltzmann constant.

During the MEFC, the freezing electric $E_{\rm fr}$ and magnetic $H_{\rm fr}$ fields are applied along the c axis. Then a single fluctuating magnetic domain can be decomposed into c-axis and ab-plane components. The magnetic susceptibility χ is an even-rank polar tensor invariant under time reversal ($+i$ symmetry), which has a $\cos^2\theta$ character. In the c-axis component, the linear ME energy and Zeeman energy terms have a $\cos\theta$ dependence. The β tensor is an odd-rank polar tensor invariant under time reversal ($-i$ symmetry); therefore the electrobimagnetic energy term will have also a $\cos\theta$ dependence. For the linear and nonlinear ME energy terms, the ab-plane projections are zero due to crystal symmetry [18,24]. We are using small electric fields, so we can ignore the energy terms of pyroelectricity PE, electric susceptibility ϵE^2, and magnetobielectricity $\gamma H E^2$. Furthermore, since $E_{\rm fr}$ and $H_{\rm fr}$ are applied along the c axis, the relevant tensor terms are only M_3, χ_{33}, α_{33}, and β_{333}, which we will refer to without indices in the following. To account for the case of an interfacial exchange coupling with an adjacent ferromagnet, such as Co, we include it using a simplistic form of an effective exchange coupling energy J_K divided by Cr_2O_3 film thickness t [5,26]. Then, the energy W for a single activation particle with a volume V is as follows:

$$\begin{aligned} W/V &= \frac{J_K}{t}\cos\theta - M H_{\rm fr}\cos\theta - \alpha E_{\rm fr} H_{\rm fr}\cos\theta \\ &\quad - \frac{1}{2}\beta E_{\rm fr} H_{\rm fr}^2 \cos\theta - \frac{1}{2}\chi H_{\rm fr}^2 \cos^2\theta \\ &\equiv W_1\cos\theta + W_2\cos^2\theta. \end{aligned} \tag{5}$$

At the threshold condition of $\langle L\rangle = 0$, there is an equal probability of a domain to be in either a L^+ or a L^- state. For this condition to hold, P_Θ becomes symmetric around $\theta = \pi/2$, and $dP_\Theta/d\theta(\theta = \pi/2) = 0$. It can be seen that the threshold condition is $W_1 = 0$ and the value of W_2 does not affect the threshold. The threshold electric field $E_{\rm th}$ is then found as follows:

$$\begin{aligned} E_{\rm th} &= \frac{\frac{J_K}{tH_{\rm fr}} - M}{\alpha + \frac{1}{2}\beta H_{\rm fr}} \\ &\approx -\frac{1}{\alpha}\left(M - \frac{J_K}{tH_{\rm fr}}\right)\left(1 - \frac{\beta}{2\alpha}H_{\rm fr}\right) \\ &\equiv A + B\cdot\frac{1}{|H_{\rm fr}|} + C\cdot|H_{\rm fr}|. \end{aligned} \tag{6}$$

In this paper, we do not use exchange-coupled films ($J_K = 0$). Therefore Eq. (6) simplifies as follows:

$$E_{\rm th} \approx -\frac{M}{\alpha}\left(1 - \frac{\beta}{2\alpha}H_{\rm fr}\right) \equiv A + C\cdot|H_{\rm fr}|. \tag{7}$$

The effect of β has a distinct qualitative feature of a linear shift in $E_{\rm th}$ by the applied $H_{\rm fr}$ during MEFC. On the other hand, the presence of M gives a constant shift in $E_{\rm th}$ [26,28]. For a bulk Cr_2O_3, both M and β are zero, and $E_{\rm th}$ is expected to be zero for all MEFC conditions. We need to note that β is invariant under time reversal. By inspecting the case in Fig. 1(b), the quadratic ME effect favors the initial parallel alignment

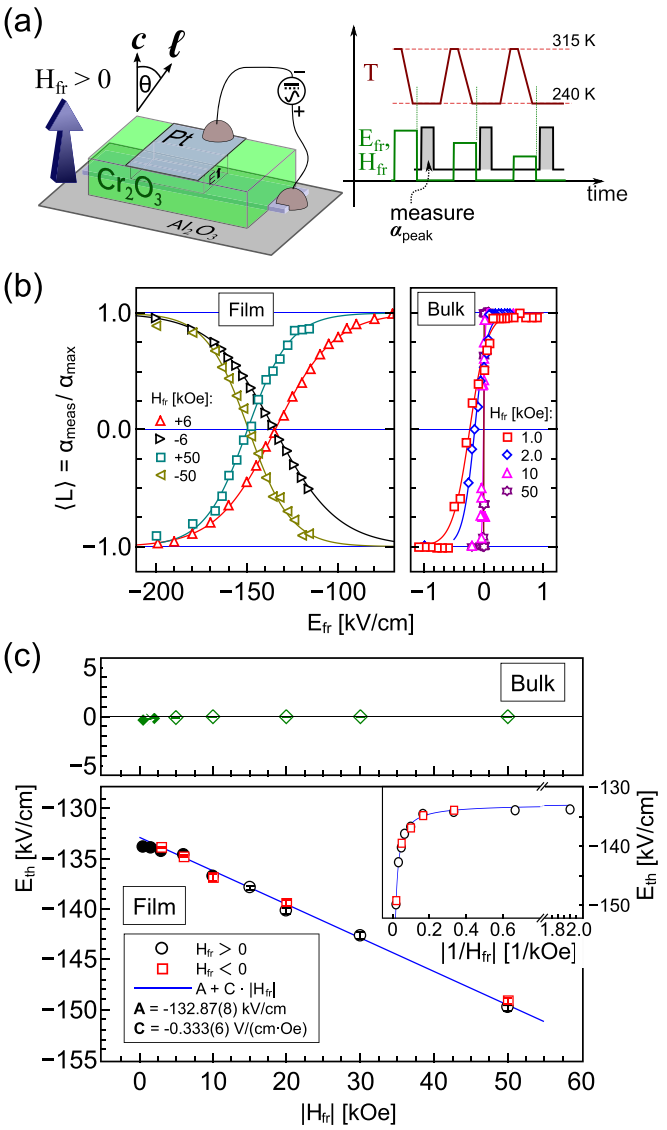

FIG. 3. (a) Schematic of the film sample and the measurement procedure. (b) The dependence of the average domain state $\langle L\rangle$ after MEFC on $E_{\rm fr}$ is shown with varying $|H_{\rm fr}|$. The solid lines are fits to a tanh function. (c) For the film sample, $E_{\rm th}$ shows a linear dependence on $H_{\rm fr}$, whereas $E_{\rm th} = 0$ for all conditions. The error bars indicate the fitting confidence, and the solid symbols are from Ref. [26]. The inset shows that there is no $1/H_{\rm fr}$ dependence.

of the M and ℓ vectors, and β will flip its sign when M changes direction under the application of the external magnetic field. Therefore the absolute value of $H_{\rm fr}$ should be used in Eq. (7).

Figure 3(a) shows a schematic of the samples and measurement procedures. To observe the quadratic ME effect, we scanned the MEFC conditions including high magnetic fields $|H_{\rm fr}| > 10$ kOe. The bulk sample is the reference sample with no expected high-order ME effects, and the film sample shows a small volume magnetization $M_s = 0.2$ emu/cm^3. After setting the temperature at 315 K, which is above T_N, the sample is cooled under various $E_{\rm fr}$ and $H_{\rm fr}$ down to the α peak temperature. Then $\langle L\rangle$ is found by normalizing $\alpha_{\rm peak}$ to its maximum value. For a fixed $H_{\rm fr}$, $E_{\rm th}$ is determined from fitting $\langle L\rangle$ to a hyperbolic tangent function [26]. The positive directions of $E_{\rm fr}$ and $H_{\rm fr}$ are along the magnetometer's positive sensing direction, as indicated in Fig. 3(a).

Figures 3(b) and 3(c) show the experimental results. After sweeping $E_{\rm fr}$ to be parallel or antiparallel to the $H_{\rm fr}$ direction, the domain state shows a transition from $+1$ (L^+ state) to -1 (L^- state) in both samples [Fig. 3(b)]. The crossing of $\langle L\rangle = 0$ occurs at the threshold condition of $E_{\rm fr} = E_{\rm th}$, as defined in Eq. (7). In the bulk sample, $E_{\rm th} \approx 0$ for all applied $H_{\rm fr}$ values, as expected due to the lack of M and β. On the other hand, in the film sample, $E_{\rm th}$ has a constant shift $A < 0$, due to the parallel alignment between M and ℓ as shown in Fig. 1(b) [26,27]. Furthermore, $E_{\rm th}$ shows a shift towards the negative side as $|H_{\rm fr}|$ is increased. The dependence of $E_{\rm th}$ on $|H_{\rm fr}|$ is plotted in Fig. 3(c), with the complementary $E_{\rm th} - |1/H_{\rm fr}|$ dependence shown in the inset. We only find a linear dependence of the $E_{\rm th}$-$|H_{\rm fr}|$ line, which is symmetric for $\pm H_{\rm fr}$, as expected from a quadratic ME effect, as shown in Eq. (7). The quadratic ME energy prefers the initial alignment of $M \parallel \ell$, and it opposes the linear ME energy during $-$MEFC. Therefore a larger negative electric field is required to switch the domain state at higher magnetic fields.

An estimation of quadratic ME susceptibility relative to the linear ME effect can be found from the slope C and intercept A of the $E_{\rm th}$-$|H_{\rm fr}|$ line. Using the fitting values in Fig. 3(c), $\beta/\alpha \approx -2 \cdot C/A = -5.0 \times 10^{-6}$ Oe^{-1}. The value of $\alpha(T_N)$ in Eq. (5) is the microscopic value, which is larger than the macroscopically observed peak value of α [26,54,55]. We estimate $\beta = -1.69 \times 10^{-18}$ s/A, based on our previous estimation of microscopic $\alpha = 27 \times 10^{-12}$ s/m [26]. In other multiferroic materials, such as $NiSO_4 \cdot 6H_2O$ [56] and $BiFeO_3$ [57], the magnitude of β is comparable to our observation, albeit reported at low temperatures of 3–4 K. Other multiferroics with a noncollinear spin structure have a large quadratic ME effect, observed at very low temperatures and high fields [10,12,58–60]. The microscopic mechanism of the quadratic ME effect in a collinear ferrimagnet requires further investigation. In the present Cr_2O_3 system, it is likely related to the same mechanism as that of the linear ME effect, namely, the two-spin symmetric exchange interaction [61,62], in combination with the removal of $\mathcal{IR}$ symmetry.

V. CONCLUSIONS

We investigated a quadratic ME effect, also called the electrobimagnetic and paramagnetoelectric effects, in sputtered Cr_2O_3 films. We found that the quadratic ME energy contributed to the ME switching during the field cooling process. The quadratic ME effects are forbidden in the magnetic point group of bulk Cr_2O_3. The emergence of this effect in films is due to removal of space-time inversion symmetry. The magnetization and Raman spectra measurements show that the space, time, and space-time symmetries are removed, likely due to site-selective doping of trace dopants in Cr_2O_3 films during growth.

Further applications to the quadratic ME effects might be found in optical rectification and frequency multiplication [16,63,64]. The magnetic point group of $3m'$ is one of the thirteen groups that allow both spontaneous electric and magnetic polarizations in addition to various ME effects [15,21,65]. Therefore we suggest that investigating and

engineering the linear and quadratic ME effect in Cr_2O_3 films will open new methods of ME control in spintronic devices.

ACKNOWLEDGMENTS

The authors thank M. Nemoto (Technical Division of Tohoku University) for technical support in the Raman spectroscopic measurements. This work was partially supported by the Center for Science and Innovation in Spintronics (CSIS) and Center for Spintronics Research Network (CSRN), Tohoku University, and the ImPACT Program of the Council for Science, Technology and Innovation (Cabinet Office, Government of Japan).

[1] A. P. Pyatakov and A. K. Zvezdin, Phys.-Usp. **55**, 557 (2012).
[2] I. Dzyaloshinskii, J. Exptl. Theoret. Phys. (U.S.S.R.) **37**, 881 (1959) [Sov. Phys. JETP **10**, 628 (1960)].
[3] D. N. Astrov, J. Exptl. Theoret. Phys. (U.S.S.R.) **38**, 984 (1960) [Sov. Phys. JETP **11**, 708 (1960)].
[4] D. N. Astrov, J. Exptl. Theoret. Phys. (U.S.S.R.) **40**, 1035 (1961) [Sov. Phys. JETP **13**, 729 (1961)].
[5] P. Borisov, A. Hochstrat, X. Chen, W. Kleemann, and C. Binek, Phys. Rev. Lett. **94**, 117203 (2005).
[6] T. Ashida, M. Oida, N. Shimomura, T. Nozaki, T. Shibata, and M. Sahashi, Appl. Phys. Lett. **104**, 152409 (2014).
[7] K. Toyoki, Y. Shiratsuchi, A. Kobane, C. Mitsumata, Y. Kotani, T. Nakamura, and R. Nakatani, Appl. Phys. Lett. **106**, 162404 (2015).
[8] M. J. Cardwell, Phys. Status Solidi B **45**, 597 (1971).
[9] S. Takano, E. Kita, K. Siratori, K. Kohn, S. Kimura, and A. Tasaki, J. Phys. Soc. Jpn. **60**, 288 (1991).
[10] E. Fogh, T. Kihara, R. Toft-Petersen, M. Bartkowiak, Y. Narumi, O. Prokhnenko, A. Miyake, M. Tokunaga, K. Oikawa, M. K. Sørensen, J. C. Dyrnum, H. Grimmer, H. Nojiri, and N. B. Christensen, Phys. Rev. B **101**, 024403 (2020).
[11] K.-C. Liang, R. P. Chaudhury, B. Lorenz, Y. Y. Sun, L. N. Bezmaternykh, V. L. Temerov, and C. W. Chu, Phys. Rev. B **83**, 180417 (2011).
[12] L. Weymann, L. Bergen, T. Kain, A. Pimenov, A. Shuvaev, E. Constable, D. Szaller, B. V. Mill, A. M. Kuzmenko, V. Y. Ivanov, N. V. Kostyuchenko, A. I. Popov, A. K. Zvezdin, A. Pimenov, A. A. Mukhin, and M. Mostovoy, npj Quantum Mater. **5**, 61 (2020).
[13] N. F. Kharchenko, Ferroelectrics **162**, 173 (1994).
[14] T. H. O'Dell, *The Electrodynamics of Magneto-Electric Media* (North-Holland, Amsterdam, 1970).
[15] A. S. Borovik-Romanov, H. Grimmer, and M. Kenzelmann, in *International Tables for Crystallography: Physical Properties of Crystals, Volume D*, 9th ed., IUCr Series, edited by C. P. Brock (Wiley, New York, 2013), pp. 106–152.
[16] H. Schmid, Int. J. Magn. **4**, 337 (1973).
[17] R. R. Birss, *Symmetry and Magnetism* (North-Holland, Amsterdam, 1964).
[18] H. Grimmer, Acta Crystallogr., Sect. A: Found. Crystallogr. **47**, 226 (1991).
[19] E. Ascher, Philos. Mag. **17**, 149 (1968).
[20] H. Schmid, Ferroelectrics **161**, 1 (1994).
[21] H. Schmid, J. Phys.: Condens. Matter **20**, 434201 (2008).
[22] V. Kopský, Symmetry **7**, 125 (2015).
[23] M. Mercier, G. Velleaud, and J. Puvinel, Phys. B+C (Amsterdam) **86-88**, 1089 (1977).
[24] H. Grimmer, Ferroelectrics **161**, 181 (1994).
[25] M. Al-Mahdawi, Y. Shiokawa, S. P. Pati, S. Ye, T. Nozaki, and M. Sahashi, J. Phys. D: Appl. Phys. **50**, 155004 (2017).
[26] M. Al-Mahdawi, S. P. Pati, Y. Shiokawa, S. Ye, T. Nozaki, and M. Sahashi, Phys. Rev. B **95**, 144423 (2017).
[27] T. Nozaki, M. Al-Mahdawi, S. P. Pati, S. Ye, Y. Shiokawa, and M. Sahashi, Jpn. J. Appl. Phys. **56**, 070302 (2017).
[28] T. Nozaki, M. Al-Mahdawi, Y. Shiokawa, S. P. Pati, S. Ye, Y. Kotani, K. Toyoki, T. Nakamura, M. Suzuki, S. Yonemura, T. Shibata, and M. Sahashi, Phys. Status Solidi RRL **12**, 1800366 (2018).
[29] See Supplemental Material at http://link.aps.org/supplemental/10.1103/PhysRevMaterials.5.094406 for the simulation of x-ray diffraction patterns and which includes Refs. [66,67].
[30] T. Kosub, M. Kopte, R. Hühne, P. Appel, B. Shields, P. Maletinsky, R. Hübner, M. O. Liedke, J. Fassbender, O. G. Schmidt, and D. Makarov, Nat. Commun. **8**, 13985 (2017).
[31] X. He, Y. Wang, N. Wu, A. N. Caruso, E. Vescovo, K. D. Belashchenko, P. A. Dowben, and C. Binek, Nat. Mater. **9**, 579 (2010).
[32] L. Fallarino, A. Berger, and C. Binek, Appl. Phys. Lett. **104**, 022403 (2014).
[33] T. Nozaki, M. Al-Mahdawi, Y. Shiokawa, S. P. Pati, H. Imamura, and M. Sahashi, J. Appl. Phys. (Melville, NY) **128**, 023901 (2020).
[34] E. Arca, A. B. Kehoe, T. D. Veal, A. Shmeliov, D. O. Scanlon, C. Downing, D. Daly, D. Mullarkey, I. V. Shvets, V. Nicolosi, and G. W. Watson, J. Mater. Chem. C **5**, 12610 (2017).
[35] T. Nozaki, S. P. Pati, Y. Shiokawa, M. Suzuki, T. Ina, K. Mibu, M. Al-Mahdawi, S. Ye, and M. Sahashi, J. Appl. Phys. (Melville, NY) **125**, 113903 (2019).
[36] J. Guo, D. E. Ellis, and D. J. Lam, Phys. Rev. B **45**, 13647 (1992).
[37] F. Rohr, M. Bäumer, H. J. Freund, J. A. Mejias, V. Staemmler, S. Müller, L. Hammer, and K. Heinz, Surf. Sci. **372**, L291 (1997).
[38] J. A. Mejias, V. Staemmler, and H.-J. Freund, J. Phys.: Condens. Matter **11**, 7881 (1999).
[39] X.-G. Wang, W. Weiss, S. K. Shaikhutdinov, M. Ritter, M. Petersen, F. Wagner, R. Schlögl, and M. Scheffler, Phys. Rev. Lett. **81**, 1038 (1998).
[40] L. Fallarino, C. Binek, and A. Berger, Phys. Rev. B **91**, 214403 (2015).
[41] P. Borisov, T. Ashida, T. Nozaki, M. Sahashi, and D. Lederman, Phys. Rev. B **93**, 174415 (2016).
[42] S. Bhagavantam and T. Venkatarayudu, Proc. Indian Acad. Sci., Sect. A **9**, 224 (1939).

[43] J. Mougin, T. Le Bihan, and G. Lucazeau, J. Phys. Chem. Solids **62**, 553 (2001).
[44] E. Kroumova, M. Aroyo, J. Perez-Mato, A. Kirov, C. Capillas, S. Ivantchev, and H. Wondratschek, Phase Transitions **76**, 155 (2003).
[45] M. I. Aroyo, A. Kirov, C. Capillas, J. M. Perez-Mato, and H. Wondratschek, Acta Crystallogr., Sect. A: Found. Crystallogr. **62**, 115 (2006).
[46] S.-H. Shim, T. S. Duffy, R. Jeanloz, C.-S. Yoo, and V. Iota, Phys. Rev. B **69**, 144107 (2004) and references therein.
[47] J. Birnie, C. Craggs, D. J. Gardiner, and P. R. Graves, Corros. Sci. **33**, 1 (1992).
[48] G. Lucovsky, R. J. Sladek, and J. W. Allen, Phys. Rev. B **16**, 4716 (1977).
[49] K. F. McCarty and D. R. Boehme, J. Solid State Chem. **79**, 19 (1989).
[50] T. Larbi, B. Ouni, A. Gantassi, K. Doll, M. Amlouk, and T. Manoubi, J. Magn. Magn. Mater. **444**, 16 (2017).
[51] Y. C. Chung and L. D. Ziegler, J. Chem. Phys. **88**, 7287 (1988).
[52] A. M. Kelley, Annu. Rev. Phys. Chem. **61**, 41 (2010).
[53] P. Appel, B. J. Shields, T. Kosub, N. Hedrich, R. Hübner, J. Faßbender, D. Makarov, and P. Maletinsky, Nano Lett. **19**, 1682 (2019).
[54] R. Ahmed and R. H. Victora, Appl. Phys. Lett. **112**, 182401 (2018).
[55] Y. Shiratsuchi, K. Toyoki, T. Yiran, H. Aono, and R. Nakatani, Appl. Phys. Express **13**, 043003 (2020).
[56] S. L. Hou and N. Bloembergen, Phys. Rev. **138**, A1218 (1965).
[57] C. Tabares-Muñoz, J. P. Rivera, A. Bezinges, A. Monnier, and H. Schmid, Jpn. J. Appl. Phys. **24**, 1051 (1985).
[58] T. Kimura, Annu. Rev. Condens. Matter Phys. **3**, 93 (2012).
[59] Y. S. Chai, S. Kwon, S. H. Chun, I. Kim, B.-G. Jeon, K. H. Kim, and S. Lee, Nat. Commun. **5**, 4208 (2014).
[60] M. Popov, Y. Liu, I. Zavislyak, H. Qu, T. Zhang, M. R. Page, and G. Srinivasan, J. Appl. Phys. (Melville, NY) **128**, 113905 (2020).
[61] M. Mostovoy, A. Scaramucci, N. A. Spaldin, and K. T. Delaney, Phys. Rev. Lett. **105**, 087202 (2010).
[62] M. Matsumoto, K. Chimata, and M. Koga, J. Phys. Soc. Jpn. **86**, 034704 (2017).
[63] K. E. Kamentsev, Y. K. Fetisov, and G. Srinivasan, Appl. Phys. Lett. **89**, 142510 (2006).
[64] M. Saito, K. Ishikawa, S. Konno, K. Taniguchi, and T. Arima, Nat. Mater. **8**, 634 (2009).
[65] M. Ye and D. Vanderbilt, Phys. Rev. B **93**, 134303 (2016).
[66] K. Momma and F. Izumi, J. Appl. Crystallogr. **44**, 1272 (2011).
[67] F. Izumi and K. Momma, in *Applied Crystallography XX*, Solid State Phenomena Vol. 130 (Trans Tech, Zurich, 2007), pp. 15–20.